Politecnico di Torino
Université Paris Cité

Master Thesis for a double degree program in:
Nanotechnologies for ICTs and Quantum Devices

Superconducting circuit for parametric coupling: development and characterization of a Josephson Parametric Converter

Laboratoire Albert Fert - mixed unit of cnrs, Thales R&T and Univeristé Paris-Saclay

Supervisor:
Dr. Danijela Marković

Candidate:
Ludovica Rizzo

Academic year 2024/2025

Acknowledgments

I would like to express my deep gratitude to my supervisor, Dr. Danijela Marković for her guidance and support throughout this entire research project and for giving me the opportunity to enter the experimental research world.

Alongside with her I would also like to thank the members of the Quantum Neuromoprhic team, whose discussions and technical advice greatly enriched my learning experience and inspired my dedication to research.

I would also like to thank Politecnico di Torino and Université Paris Cité for offering me the great opportunity to undertake this double-degree program in France.

A special thank you goes to my colleagues from Politecnico di Torino and NANOQUAD project, for all the shared moments and the help they gave me during these two years, both in France and Italy.

Finally, I would like to thank my family for always being there form me, supporting me and offering me advises throughout my academic and personal journey, both in good times and difficult ones.

Abstract

This thesis explores the implementation of quantum neural network using superconducting circuits, with a focus on improving the quality factor of coplanar waveguide resonators and demonstrating parametric coupling for quantum information processing.The work was conducted at Laboratoire Albert Fert under the supervision of Danijela Marković , involving both the design optimization and experimental characterization of superconductive architectures. In particular, Josephson Parametric Converters (JPC) were fabricated and their performances were explored in cryogenic environments in order to investigate their suitability for quantum neural network applications. The key results include realization of high-quality factor resonators ($Q > 10^4$), as well as observing parametric coupling phenomena through two-mode squeezing and coherent photon conversion, performed by three-wave mixing procedure. These findings support the potential of superconducting circuits as scalable hardware for quantum neuromorphic computing.

Contents

1 Introduction and background

1.1 From biological to Artificial Neural Network

The morphology and physiology of the human brain have evolved to meet the demanding requirements of efficient, high-capacity information processing and advanced cognitive functioning while maintaining remarkable energy efficiency. Understanding the fundamental mechanisms by which biological neural networks achieve such exceptional performance represents a major breakthrough in next-generation artificial intelligence development. Such insights would lead to significant improvements in the efficiency and capabilities of current machine learning algorithms [8]. The remarkable efficiency of biological neural networks has motivated researchers to develop neuromorphic computing, a paradigm implementing physical neural networks inspired by brain architecture and the way of processing information, leading to the birth of Artificial Neural Networks (ANN). Unlike traditional algorithms, ANN learn directly from large datasets that serve as examples, allowing the network parameters to be learned rather than explicitly programmed.

ANN are parametrized mathematical models able to reproduce complex probability distribution of the underlying example datasets.They consist of layers of artificial neurons, that are non linear functions, interconnected through synaptic weights. Three primary layers can be identified in an ANN (their arrangement is shown in Figure 1):

- Input layer: receives input data used for the training of the learnable parameters.
- Hidden layers: intermediate computational layers where the learning occurs. Each neuron applies weighted sum of the inputs followed by a non-linear activation functions enabling the network to learn and generalize complex pattern. Weights are the strengths of neurons interconnections, synapses, between each of the hidden layers and they are the parameters adjusted during training.
- Output layer: produces the model's predictions or classification result.

The fundamental operations within a neural network are:

- Linear transformation: the equivalent of the synaptic integration in biological neurons, performed by synapses.
- Non-linear activation: application of a non-linear function (e.g. ReLu, sigmoid) necessary since all the real-world information are non-linear, so only linear transformation will make it impossible to model more complex tasks, such as image recognition. These non-linear activation functions are applied by the neurons on the input data. They are used to adapt the synaptic values through learning rules based on loss function, backpropagation and gradient descent.

Combining these two aspects, the parameters (weights) are adjusted during training by analyzing examples, allowing the network to "learn" by processing numerous input data. As said, the main learning rules are based on backpropagation and gradient descent. This means

that after measuring the error on the output prediction, the weight that most impacted on it is calculated and it is updated proportionally to the impact it had on the error. The process stops when the correct prediction probability has been maximized.

This being said, if classical neural network algorithm are doing the job and are doing it good, where does the need and curiosity in adding a quantum physics component to it comes from?

1.2 Quantum Neural Network

In order to properly emulate brain capability of information manipulation, neural networks need to fit highly complex functions. This requires both a high number of neurons, dense connections among them and long memory. To answer these requirements, classical hardware reaches a bottleneck in terms of energy consumption and device scalability. It is at this point that quantum neural networks become interesting.
Quantum mechanics naturally provides the scalability and strong non-linearity needed for neural networks. Indeed, quantum systems allow to encode neurons not in the individual physical devices (number of neurons linearly tied to the number of physical units), but in the basis states. With this approach, the number of neurons is exponential with the number of individual devices. With N available physical components and M accessible states per component, we can obtain up to M^N neurons, creating a higher-dimensional state space and enabling high numbers of neurons without increasing hardware complexity. For example, simulations carried out in the hosting research group (see Ref.[1]) have demonstrated that using only two coupled quantum oscillators - each supporting 9 measurable states - the number of effective neurons rises to 81, showing how small quantum systems are capable of emulating large-scale network behavior due to their intrinsic high-dimensional nature.
This become possible thanks to two key quantum phenomena that redefine neural network implementation:

- Superposition, which allows to encode multiple computational states in a single quantum system.
- Entanglement, which introduces non-classical correlation among quantum neurons that cannot be reproduced by classical system; the analogous to learnable weights in ANN.

These unique properties enable fundamentally new paradigms for information processing and encoding. Their implementation does not just improve classical computational tasks efficiency, but also opens the door to completely new, intrinsically quantum tasks, non solvable with classical computers.

One of the key issues in realizing Quantum Neural Networks (QNN) lies in the physical implementation of adaptable interactions, analogous to classical weight tunability. This is were parametric coupling plays a crucial role.

1.3 Parametric coupling: a tool for tunable quantum interactions

Traditionally inter-mode coupling within quantum systems can be achieved through capacitive or inductive coupling. However this methods suffer from a strong limitation: the coupling strength, that is the equivalent of a trainable weight, is fixed form fabrication and remain static during the entire operation of the system.
A dynamically tunable interaction mediated by nonlinear elements is instead offered by parametric coupling. The coupling strength between modes can be continuously adjusted via external parameters (e.g., pump frequency, pump power, flux bias) and can be selectively activated or deactivated, enabling a reconfigurable network. Making use of nonlinear elements, such as Josephson junctions, it moreover provides entanglement, squeezing and photon conversion through strong processes like three-wave mixing.

The training of such parametric interaction is what the Quantum Neuromorphic team at Laboratoire Albert Fert, where my internship took place under the supervision of Danijela Marković, is working on: the simulations have already been successful [4] while experimental implementation is just starting, using superconducting circuits. The goal of my internship was to improve the quality factor of superconducting architectures, so to extend the coherence time of the modes involved, and to introduce tunable parameters using parametric coupling, observable through two-mode squeezing and coherent photon conversion between two quantum oscillators using a three-wave mixer. To translate this theoretical advantages in practice, other colleagues in the team were working on the same topic: Baptiste Carles, a second-year PhD student was working on the experimental implementation of a quantum reservoir using a superconducting cavity, Briac Flesselles, the other intern on our team, was designing transmon qubits to be coupled with a Josephson Parametric Converter (JPC) for basis state readout and Julien Dudas, the other PhD student, worked on simulations of quantum reservoir computing with bosonic modes and on training the parametric interactions in analog bosonic QNN with Fock basis measurements.

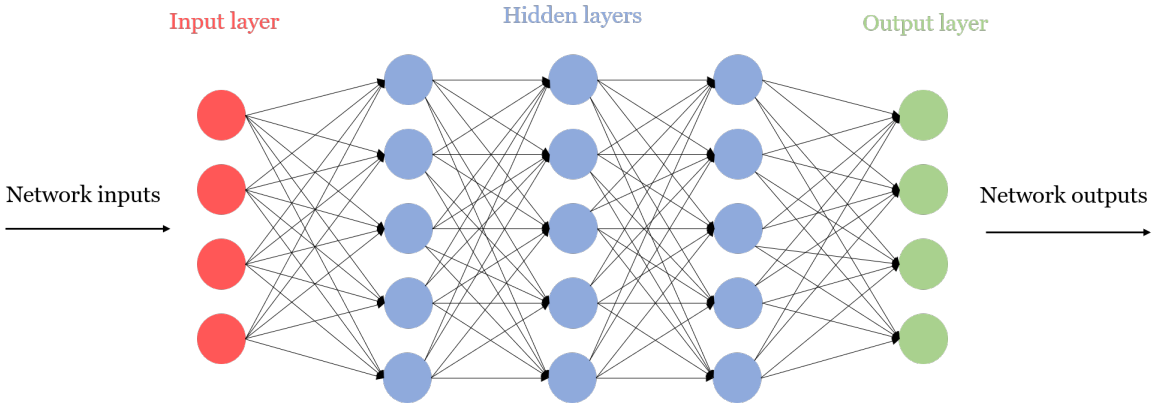

Figure 1: Schematic of an Artificial Neural Network where the circles represent the neurons, which apply the nonlinear function, interconnected by synapses, represented as arrows, which apply the weight multiplication.

2 Objectives and device choice

The main objective of this internship was to use superconducting architectures - a Josephson Parametric Converter (JPC) - to implement and experimentally characterize parametric coupling between harmonic oscillators, realized through two superconducting resonators modes. This capability allows to use bosonic modes as neurons and their interactions strength as synaptic weights.
The project work focused on three keys goals:

- Reduce the fundamental resonance frequency of coplanar waveguide (CPW) resonators to bring multiple harmonics (e.g., $\lambda/2$ and $3\lambda/2$ modes) in the working frequency range.
- Improve the quality factor of the resonators, extending the coherence times and enhancing the memory capacity of each mode - essential requirement for temporal and recurrent neural tasks.
- Demonstrate parametric coupling between the existing modes, using a three-wave mixing element.

To answer this requirements I worked on design, fabrication and cryogenic characterization of three different generations of superconducting devices, each introducing improvements steps towards the final working device, the JPC.
Given the existence of alternative bosonic systems (opto-mechanical resonators, optical cavities), the first question to answer to is: why do we need superconducting circuits?

2.1 Superconducting architectures for Quantum Neural Networks

The development of Quantum Neural Networks requires hardware platform able to provide high-dimensional state space, controllable nonlinearities and long memory. To answer this requirement, superconducting circuits stand out due to their ability of integrating coplanar waveguide (CPW) resonators on-chip with Josephson junctions, the key component providing the necessary non-linearity, even at a single photon level, and strong parametric coupling, thus the tunable interaction we were looking for training QNN. These junctions, made of a layered structure $Al/AlO_x/Al$, introduce some anharmonicity in the system Hamiltonian due to their cosine dependence on an external applied flux, which enables interaction terms beyond simple linear dynamics:

$$H_{JJ} = -E_J \cos\left(\frac{2\pi\hat{\Phi}}{\Phi_0}\right) \tag{1}$$

where $\Phi_0 = \frac{\hbar}{2e}$ is the reduced flux quantum enabling the photon-photon interaction, Φ is the external flux and E_J is the energy of the junction and it is proportional to the junction surface and geometry and to its critical current I_0.

I started from the current state of the art device in the group that hosted me - the Josephson Parametric Converter (JPC). JPC is composed of two crossed superconducting resonators coupled via a Josephson Ring Modulator (JRM) at the central crossing point. This device

leverages the nonlinearities to perform three-wave mixing, facilitating the two-mode squeezing and coherent photon conversion processes involved in parametric coupling. The resonators instead support multiple electromagnetic modes behaving as slightly anharmonic quantum oscillators, whose frequencies are tunable through geometric parameters:

$$f_0 = \frac{c}{\sqrt{\epsilon_{eff}}} \frac{1}{2l} \tag{2}$$

where f_0 is the fundamental mode frequency for a $\lambda/2$ resonator, c is the speed of light, ϵ_{eff} is the effective permittivity and l is the resonator length. Every resonator has an inductance L_l and capacitance C_l that depend mostly on their geometry. From these information we can deduce that a resonator can be modeled with and electric schematic that is the one of an LC oscillator (no R since superconducting) [7]. This will help in understanding the effect of the resonators geometry and electrical parameters on the coupling and thus on the quality factor and resonant frequency.

This being said, the advantage of using this kind of superconducting circuit lies in the on-chip scalability and precise parameter control through the JRM. Indeed, Josephson junctions implement tunable coupling strength through an external flux bias in a three-wave mixing element - the JRM.

2.1.1 Josephson mixer dynamics

Having all the important information about resonators, we can describe how their modes are coupled. Simple proximity coupling (capacitive or inductive) is possible but it lacks tunability, so to have control over parametric coupling between oscillators (get the two mode squeezing and coherent photon conversion in quantum systems) an already existing device was employed: the Josephson parametric converter (JPC) - a three wave mixer. It is made of two crossing superconducting resonators with a Josephson Ring Modulator (JRM) at the crossing point. The JRM is made of four Josephson junctions in a Wheatstone bridge configuration, made of superconductor-insulator-superconductor layered structure, corresponding to a non-linear inductance modulated by the geometry of the junctions and by the magnetic flux bias crossing the ring (for a deeper and complete insight on this topic see Flurin thesis [3] from which I am taking inspiration for the model description).

To this junctions configuration we can associate the following inductances and Hamiltonian:

$$L_{X,Y}^{JRM} = \frac{\varphi_0}{I_0 cos\left(\frac{\tilde{\varphi}_{ext}}{4}\right)} \qquad \text{and} \qquad L_Z^{JRM} = \frac{\varphi_0}{4I_0 cos\left(\frac{\tilde{\varphi}_{ext}}{4}\right)} \tag{3}$$

$$\begin{aligned} H_{\text{ring}} = & -4E_J \cos\left(\frac{\tilde{\varphi}_{\text{ext}}}{4}\right) + \frac{1}{2}E_J \cos\left(\frac{\tilde{\varphi}_{\text{ext}}}{4}\right)(\varphi_X^2 + \varphi_Y^2 + \varphi_Z^2) \\ & \underbrace{- E_J \sin\left(\frac{\tilde{\varphi}_{\text{ext}}}{4}\right)\varphi_X\varphi_Y\varphi_Z}_{\text{three-wave mixing}} + \mathcal{O}(|\varphi|^4) \end{aligned} \tag{4}$$

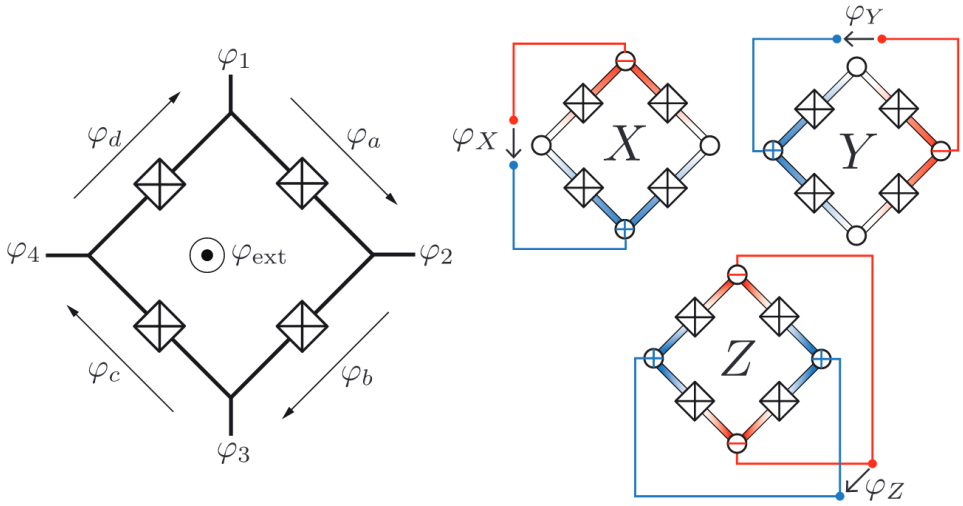

Figure 2: The Josephson Ring Modulator (JRM) consisting in four Josephson junctions in a Wheatstone bridge configuration (on the left). Representation of the normal modes symmetry of the ring (on the right). The picture is taken from [3].

where $\tilde{\varphi}_{ext} = \varphi_{ext} + 2n\pi$ and L_X, L_Y and L_Z are the inductances of the ring in each direction. The modes in the ring, in each direction, assume a different symmetry configurations, which are observable in Figure 2, and flux distribution. Furthermore, they are associated with different current paths through the junctions and respond differently to the external magnetic flux. These inductances should be added to the resonators ones, once the ring is introduced in the design, lowering the effective resonance frequencies, introducing a flux tunability to the system dynamics. The strength with which each resonators mode couples to the JRM energy is quantified by the participation ratio:

$$\xi_\mu(\varphi_{ext}) = \frac{L_\mu^{JRM}(\varphi_{ext})}{L_\mu^{tot}} = \frac{L_\mu^{JRM}(\varphi_{ext})}{L_\mu + L_\mu^{JRM}(\varphi_{ext})} \tag{5}$$

From 3 and 5 it is easily observable that the inductances depend on the external flux action on the devices and thus being $\omega_\mu^0 = \frac{1}{\sqrt{L_\mu^{tot} C_\mu}}$ also resonators resonance frequency is modulated through it as:

$$\omega_\mu(\varphi_{ext}) \approx \omega_\mu^0 \left(1 - \frac{1}{2}\xi_\mu(\varphi_{ext})\right) \tag{6}$$

From all of these information the Hamiltonian of the system can be obtained as:

$$H = \hbar\omega_a \hat{a}^\dagger \hat{a} + \hbar\omega_b \hat{b}^\dagger \hat{b} + \hbar\chi(\hat{a} + \hat{a}^\dagger)(\hat{b} + \hat{b}^\dagger)(\hat{c} + \hat{c}^\dagger) \tag{7}$$

in which the three-wave mixing part is expressed in the last term, defined by the coupling factor χ that depends on the participation ratio of all the modes involved in the mixing and $\hat{c}$ denotes the common mode.
Since it is often used as a pump a better description of the common mode properties must

be given:

$$\begin{aligned} L_C &= \frac{1}{4}\left(L_a + L_b\right) \\ C_c &= \frac{4C_aC_b}{C_a + C_b} \\ \omega_c &= \frac{2\omega_a\omega_b}{\omega_a + \omega_b} \end{aligned} \tag{8}$$

This mode is thus distributed in the two resonators and when it is maximum in one, it is minimum on the other, giving an anti-phase behavior between them.

2.1.2 Kerr effect

Since the primary goal of this project is to harness three-wave mixing for parametric coupling, the Hamiltonian in eq. 7 takes into account only nonlinearities up to the third order; a further development in the degree of nonlinearities will results in the appearance of a photon-number dependent one. That is the Kerr effect, a fourth-order interaction resulting in a frequency shift in the resonators modes. This effect naturally arises in Josephson junction based system due to the non-parabolic nature of the cosine potential (eq. 1), so it can actually be used as a way to probe the activity and participation of the ring junctions in the coupling process. Developing beyond the third order the ring Hamiltonian the Kerr nonlinearity contribution must be added:

$$H_{Kerr} = \hbar K_{aa}\left(\hat{a}^\dagger\hat{a}\right)^2 + \hbar K_{bb}\left(\hat{b}^\dagger\hat{b}\right)^2 + \hbar K_{ab}\hat{a}^\dagger\hat{a}\hat{b}^\dagger\hat{b} + \hbar K_{ac}|p|^2\hat{a}^\dagger\hat{a} + \hbar K_{bp}|p|^2\hat{b}^\dagger\hat{b} \tag{9}$$

This effect represents a four-wave mixing effect that we want to avoid so to focus our attention on the stronger three-wave mixing process and introduces unwanted frequency shifts and nonlinear dispersion that may interfere with the operations of amplification and conversion, degrading coupling strength. Since it is power and flux dependent we should consider it while performing our analysis.
In the equation above three kind of terms may be recognized:

- Self Kerr terms $K_{\mu\mu}$ that involve only one mode and produces a shift in the resonance frequency that is proportional to the number of photons in the field. Those terms should produce a more pronounced effect at higher applied input signal.
- Cross-Kerr terms K_{ab} which involves both resonator modes and induces a frequency shift on one of them proportionally to the photon population of the other.
- Pump induced-Kerr terms $K_{\mu p}$ arising from strong driving fields.

A more detailed description of this effect can be found in [2]).

3 Analysis and results

The experimental phase of this internship involved design, fabrication and characterization of multiple generations of superconducting circuits, each aiming at improving device performances and enabling the parametric coupling. Three generations of samples were developed and analyzed, each addressing one of the main goals of my internship. The evolution of these generations followed a systematic optimization strategy culminating in a working final architecture exploiting the wanted features.

3.1 First generation: JPC 1 and JPC 2

Samples of the first generation - JPC 1 and JPC 2 - have been used to assess ground plane role in the quality factor improvement. Magnetic vortices formation in the ground plane can induce coherence losses. These may cause the reduction of the coherence time of resonators modes, that need to be high due to the required memory in Quantum Neural Network. For this reason ground plane holes were added to the design of the samples. Both samples of this generation presented straight resonators but further details about their design are given in Figures 3 and 4.

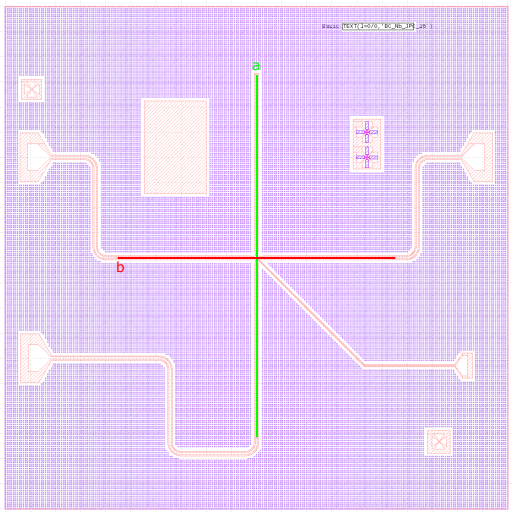

Figure 3: Design of JPC 1 consists of two resonators with fundamental modes at 8.5 GHz (a arm in green) and 10.5 GHz (b arm in red). One resonator was terminated by an open end and the other is capacitively coupled to a contact pad. The JRM was unshunted, with 10x15 μm^2 footprint and 0.4 μm junction bridge width and 1.3 μm junction bridge length. This sample also presents two test JRMs for room temperature junction resistance characterization, a DC flux line for flux biasing and alignment crosses.

To better understand the results obtained on these samples we need to consider that quality factor depends on different parameters that must be taken into account while improving it, we briefly describe them in the following.

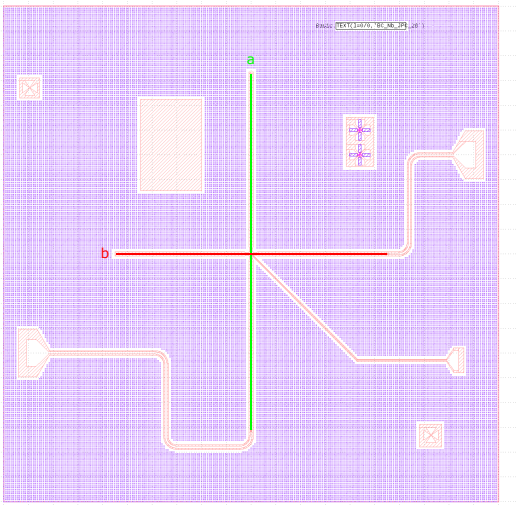

Figure 4: Design of JPC 2 consits of two resonators with fundamental modes at 8.5 GHz (a arm in green) and 10.5 GHz (b arm in red) target frequency. Both resonators are terminated by an open end to analyze boundary conditions effects on resonator behavior. Same implementation of the JRM, test JRMs and alignment crosses as in JPC1 are kept. DC flux line was short circuited by a scratch.

3.1.1 Quality factor

In order to be able to address them, the resonators are capacitively coupled to a transmission line. The coupling was realized with interdigitated capacitors. This design provides high coupling efficiency, via small capacitive gaps between microstrip feed lines and microstrip resonators.
The coupling factor κ_{ext} is defined through the matched line impedance $R_L = 50\ \Omega$, in series with the coupling capacitance C_k (See Figure 5 for the representation of the capacitive element). Since the entire circuit can be described with a Norton equivalent we can define R^* and C^* as the loads of the line and supposing a weak coupling regime, meaning $\omega_n C_k R_L \ll 1$ with ω_n the n-th mode frequency, we can define the external coupling and quality factors of the device:

$$\begin{aligned} \kappa_{ext} &= \frac{R_L \omega_0^2 C_k^2}{C} = R^* C \\ Q_{ext} &= \frac{\omega_0}{k_{ext}} \end{aligned} \tag{10}$$

Other than external interactions, also internal losses must be considered. If the external losses can be predicted since they are associated to electrical and geometrical properties of the device, the internal ones can not, being due mainly to fabrication imperfections and cleanliness. The associated factor to these losses is:

$$\begin{aligned} \kappa_{int} &= RC \\ Q_{int} &= \frac{\omega_0}{\kappa_{int}} \end{aligned} \tag{11}$$

From the coupling factor and loss term we can define the overall quality factor of the device:

$$\frac{1}{Q} = \frac{1}{Q_{ext}} + \frac{1}{Q_{int}} \tag{12}$$

and from here define the coupling coefficient $g = \frac{Q_{int}}{Q_{ext}}$ that gives us an idea of the coupling strength, combining both the effects:

- g > 1 resonator is overcoupled and $\kappa_{ext} \gg \kappa_{int}$ and the quality factor strongly depends on the coupling capacitance.
- g = 1 the resonator is critically coupled and optimal transmission is reached.
- g < 1 the resonator is undercoupled and $\kappa_{ext} \ll \kappa_{int}$ and in this case the transmission is drastically reduced.

The goal is to achieve quality factor higher than 10^4 so to have long coherence time, meaning $T = \frac{Q}{\omega} > 10^{-5}$ s since we are working with microwaves modes in the GHz range, and very thin and well-defined modes, meaning $\Delta\omega = \kappa_{ext} + \kappa_{int}$ in the order of hundreds of kHz or at most few MHz. This will allow for easily distinguishable modes, so to be able to address a single oscillator.

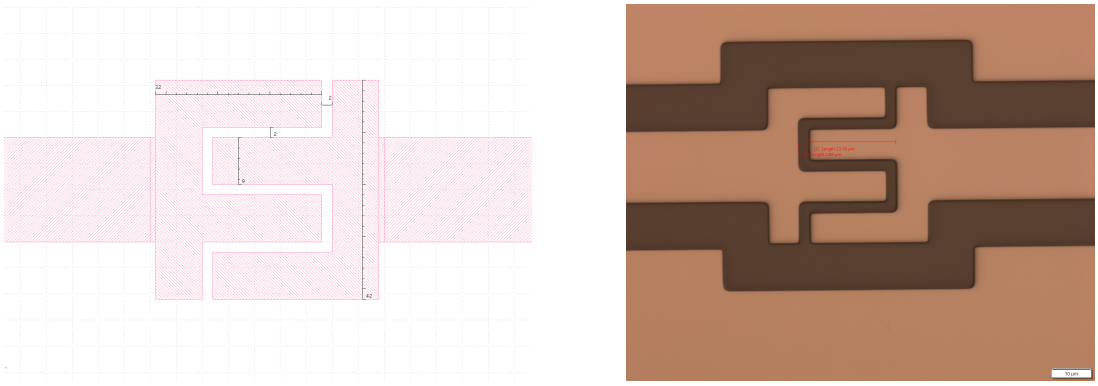

(a) Coupling capacitance design (b) Coupling capacitance after optical lithography

Figure 5: Capacitive coupling element between the transmission line and the resonator presented in a) design form and b) optical lithography result. The gap between each finger of the interdigitated capacitor is 2 μm wide.

3.1.2 Results

To characterize the devices we used a Vector Network Analyzer (VNA) to measure the reflection coefficient at low temperature

$$r[\omega] = \frac{\kappa_{ext} - \kappa_{int} + 2i(\omega - \omega_0)}{\kappa_{ext} + \kappa_{int} - 2i(\omega - \omega_0)}. \tag{13}$$

The VNA sends RF signals and measures then the reflected signal amplitude and phase comparing it with the input. Thanks to eq. 13 we are able to extract from the measured values

the internal loss rate and external coupling rate and in the case in which $\kappa_{ext} > \kappa_{int}$ a 2π phase shift is acquired by the signal at the resonance frequency. The spectral width of the resonance is given by $\kappa_{ext} + \kappa_{int}$.
When the input signal is sent in the circuit, it has two possible reflection paths: the resonant one inside the resonator where it interact with the mode of interest, or a background one in which the signal is reflected by some other components (ground plane, connectors,...). If these two paths interfere, the interference modifies the shape of the resonance producing an asymmetric line-shape - the signature of a Fano reflection (insights on this topic can be found in Ref. [5]). The $r[\omega]$ coefficient is modified due to some interferences in the reflected signal in $r_{Fano} = (1-b)r[\omega] + be^{\varphi}$. Using both relations for the reflection coefficient we can obtain resonance frequency, losses and coupling factors of each resonators.
In the following, we will apply an external magnetic field to the JPCs in order to characterize their dependence on flux. We will use the reflection coefficient in eq. 13 and Fano reflection coefficient to extract the resonance frequency at each flux.

JPC 1
With sample JPC 1 we were trying to address only one mode on each resonator in the range 8-11 GHz with one of the arm of the JPC having an open end and the other arm ending on a contact pad. On this design a JRM with surface 10x15 μm^2 has been implemented. Looking at Figure 3 the green - *a* - arm is the longest one corresponding to the shorter $\lambda/2$ mode at 8.5 GHz, while the red - *b* - arm is the shorter so has the higher frequency mode at 10.5 GHz.

Measuring this sample inconsistent modes were observed with respect to the targeted frequencies. From the data in table 1 it is observable that some modes at the right frequency

Resonator	Expected frequency (GHz)	Frequency (GHz)	κ_{ext} (kHz)	κ_{int} (kHz)	Kerr effect	Flux dependence
a arm		6.765	858.263	6466	no	yes
a arm	8.5	8.56	2913	8890	yes	-
b arm		8.56	917.157	3774	yes	no
b arm	10.5	9.7	-	-	-	yes

Table 1: Modes on JPC 1. The appearing modes are not the expected ones. There was one mode per each arm of the JPC that seems to reflect the target frequencies, but some of them were observable only under a pump signal application. Moreover resonators seems to be a bit undercoupled, reducing the transmission efficiency.

appears, but on *a* arm they were visible only under pump excitation, suggesting some fabrication irregularities. The modes observed on *b* arm instead showed the expected power dependence, but with low quality factor and undercoupling, meaning both κ_{ext} and κ_{int} of the order of some MHz, bringing the Q value in the order of 10^3. Furthermore these modes showed irregular shapes that did not allow for a proper analysis of the reflection coefficient, especially on the arm that required the pump signal to observe the modes, as can be seen in

Figure 6, where the fit and raw data curves do not overlap perfectly.

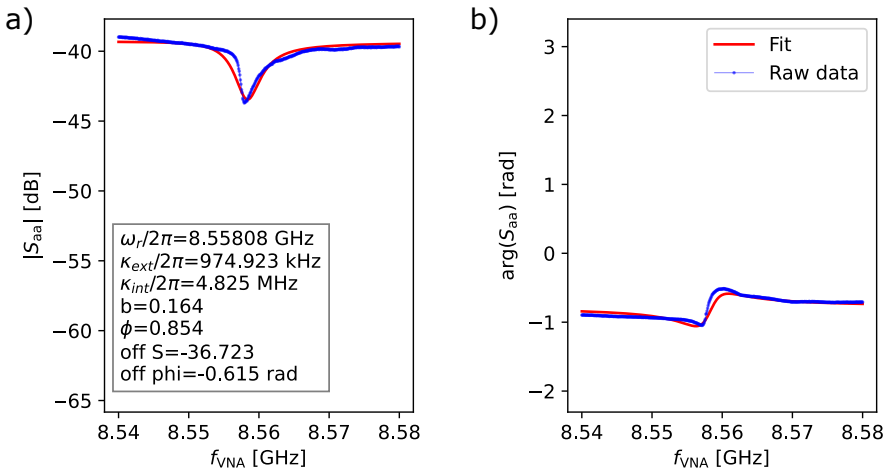

Figure 6: Single trace of a) amplitude and b) phase of the measured reflection coefficient (blue) and fit (red) from Fano reflection expression on JPC1 mode at 8.56 GHz. It allowed to extract resonance frequency ω_r, internal losses κ_{int}, external coupling κ_{ext}, amplitude $off\ S$ and phase $off\ phi$ offsets and b Fano correction factor.

JPC 2

On sample JPC 2 the only difference with respect to the previous sample is the fact that both resonators have one open end and one end capacitively connected to a contact pad. The obtained results are presented in Table 2.

Resonator	Expected frequency (GHz)	Frequency (GHz)	κ_{ext} (kHz)	κ_{int} (kHz)	Kerr effect	Flux dependence
a arm	-	6.3431	671	1490	yes	no
a arm	8.5	8.52204	737.6	788.1	yes	no
a arm	-	11.37738	453.7	782.9	no	no
b arm	-	6.34302	891.5	1734	yes	no
b arm	-	7.87045	995.3	2000	no	no

Table 2: Modes on JPC 2. The appearing modes are not the expected ones, only one mode on a arm seems to reflect the target frequency, while on b none of the observed frequencies corresponds to the implemented 10.5 GHz. Moreover resonators seems to be a bit undercoupled, reducing the transmission efficiency.

As can be seen from the data in Table 2, the resonators result in being slightly undercoupled, reducing so the transmission efficiency. Despite that the quality factor Q_{ext} seems to be in the right range of order of magnitude (κ_{ext} and κ_{int} are both of the order of kHz), unfortunately, the modes observed during the measurement are not the expected one at all.

A range of harmonics appeared and it was not clear which one of them was the right mode that we were trying to address. Indeed on a arm a frequency close to the expected 8.5 GHz was found, but the other two were not compatible with any other possible mode on that resonators ($3\lambda/2 = 25.5$ GHz). About the b arm instead, the targeted frequencies was not reached by neither of the observed modes. As a further step the flux dependence was obtained with an external magnet since the DC flux line was short circuited by a scratch during fabrication, but no variation in the reflection coefficient was observed.

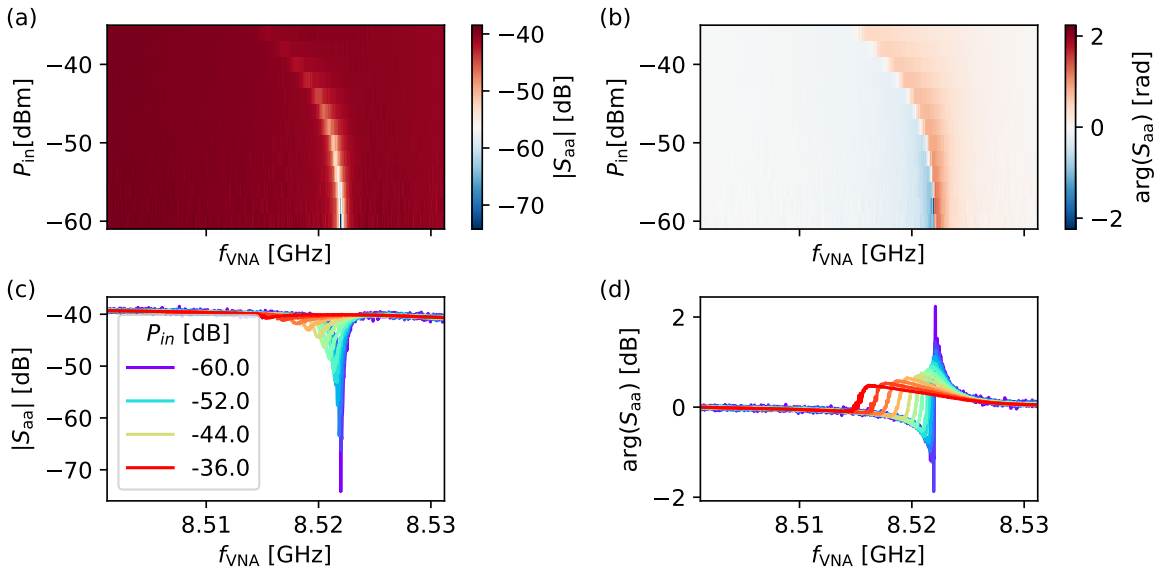

Figure 7: Reflection coefficient measurement on JPC2. All four figures show the mode at 8.52 GHz. (a) Reflection coefficient magnitude as a function of the input power and frequency. The blue color corresponds to a dip in the reflection coefficient, identifying the frequencies at which the transmission is the highest and reflection the lowest, thus the resonance frequency. (b) Phase of the reflection coefficient where a 2π shift is visible at the resonance frequency. (c) Amplitude and d) phase of the reflection coefficient as a function of the frequency. Power dependence is presented as curves of different colors for different input signal powers. In both representation the frequency shift is clearly observable, highlighting the presence of some Kerr effect and thus the participation of the Josephson junctions to the mode.

From Figure 8 it is observable that the characterization of the resonators mode using eq. 6 gives reasonable values of κ_{ext} and κ_{int} of the order of hundreds of kHz . This can be justified also from the fact that more or less the sum of this two values should correspond to the width of the observed mode, that corresponded to fluctuations around the central peak of about 1 MHz. Moreover the values of the offsets S and Φ in amplitude and phase in the reflection coefficient due, respectively, to a missing compensation of attenuation to amplification in the input/output line and to a dephasing due to different time needed by the signal to go through the circuit at different frequencies can be obtained from the same figure. From Figure 7 instead it is noticeable the presence of Kerr effect under a power sweep both in the amplitude and phase representation of the reflection coefficient, confirming JRM

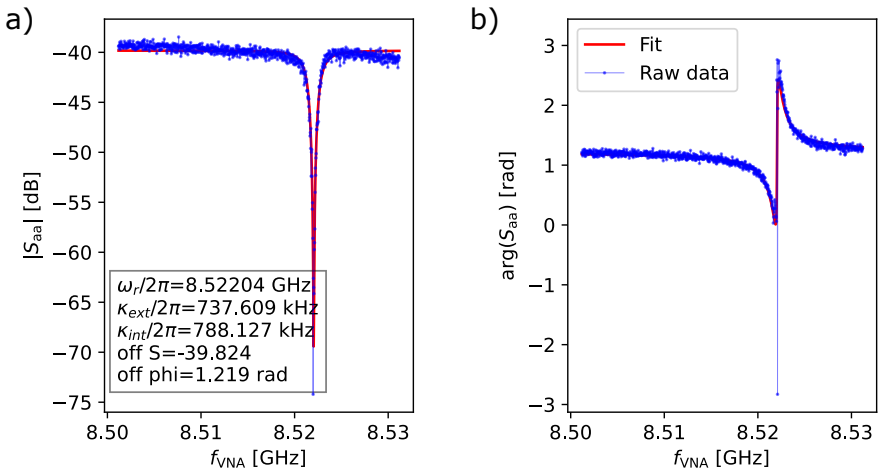

Figure 8: Single trace of a) amplitude and b) phase of the measured reflection coefficient (blue) and fit (red) from eq.13 on JPC2 mode at 8.52 GHz at input power -60 dBm, allowed to extract resonance frequency ω_r, internal losses κ_{int}, external coupling κ_{ext} and amplitude $off\ S$ and phase $off\ phi$ offsets.

participation to resonators mode.
Although the target frequencies were not reached and the resonators were undercoupled, the experiment validated the improvement in the quality factor brought through ground plane holes. This findings motivated a shift in the strategy for next generation samples: a focus on single resonators geometry optimization was proposed, with the intention of addressing the right frequencies and lowering the working frequency range. The lower frequency range in 3-15 GHz will allow to address more than one mode per each resonator considering the working range of our cryogenic measurement instruments - circulators and amplifiers in the cryostat operate at 4-12 GHz range.

3.2 Second generation: RES1 and RES2

The second sample generation was designed to overcome the limitations encountered in the first experiments - particularly the mismatch in the expected and observed resonance frequencies. In this iteration the focus shifted to optimizing the isolated resonators geometry with the goal of achieving:

- Lower resonance frequency for the fundamental mode, so to bring multiple harmonics within the accessible bandwidth range of 3-15 GHz. In this way two modes on each resonators could be addressed at $\lambda/2$ and $3\lambda/2$ wavelength, making 4 harmonic oscillators available for parametric coupling.
- Higher external quality factor Q_{ext} and thus lower κ_{ext}, reaching the overcoupling to get good transmission in the devices.

To meet these goals, looking at eq. 10 and 2 the solution was to increase resonators length, incorporating a meandered design that helped minimizing the longitudinal extension of the

devices, so to fit them in a 10x10 mm^2 sample, and reducing the overall resonator inductance due to some internal one generated among the meanders.
These design changes are performed and studied in samples Res 1 and Res 2 whose design is shown in Figures 9 and 10.

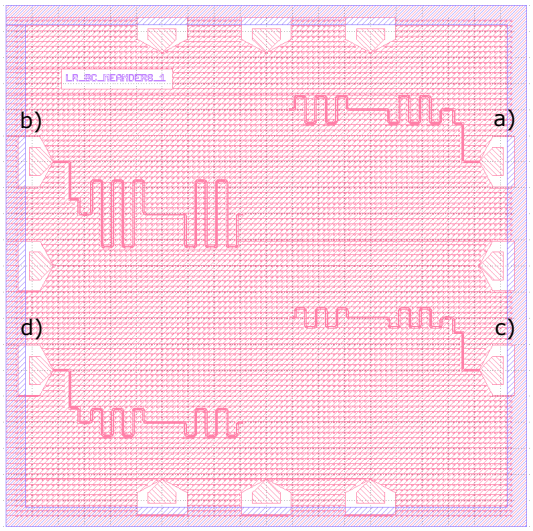

Figure 9: Design of Res1 consists of four resonators, targeting 8 GHz (a, d), 4GHz (b) and 10 GHz (c), with varying length to asses the impact of the meandered geometry on different fundamental mode frequencies. Due to dust particles and scratches on resonators a and b, they were not functioning. An external ring (in purple) was added to increase the exposure dose during optical lithography in this region to help the contact pads development, though it produced no observable improvement.

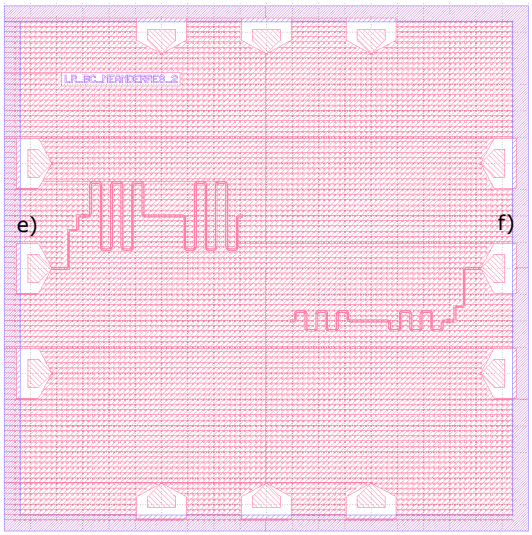

Figure 10: Design of Res 2 consists of two resonators targeting 4 GHz (e) and 10 GHz (f). On this sample the external ring (in purple) to increase the exposure dose during optical lithography to help the contact pads development was also added since the two samples were produced contemporarily.

3.2.1 Results

Res 1

On sample Res 1 only two out of four resonators were working due to some dust particles and scratches short circuiting two of them, leaving only one at 8 GHz, Res 1 d, and one at 10 GHz, Res 1 c, available for analysis.

The most interesting result from this sample, other than correctly addressing the targeted frequencies, was the presence of Fano reflection features on both the measured resonators, that can be mostly due to some fabrication defect or other imperfections that may have caused some interferences in the reflection path of the signal (an example can be seen in Figure 11).

Resonator	Expected frequency (GHz)	Frequency (GHz)	κ_{ext} (kHz)	κ_{int} (kHz)	b
d	8	7.98831	1526	433.954	0.256
c	10	9.97101	4404	442.922	0.104

Table 3: Modes frequency on sample Res 1. Values of κ_{ext} an κ_{int} have been obtained by fitting the measurement through eq. 6 and b represent the correction factor introduced by Fano reflection.

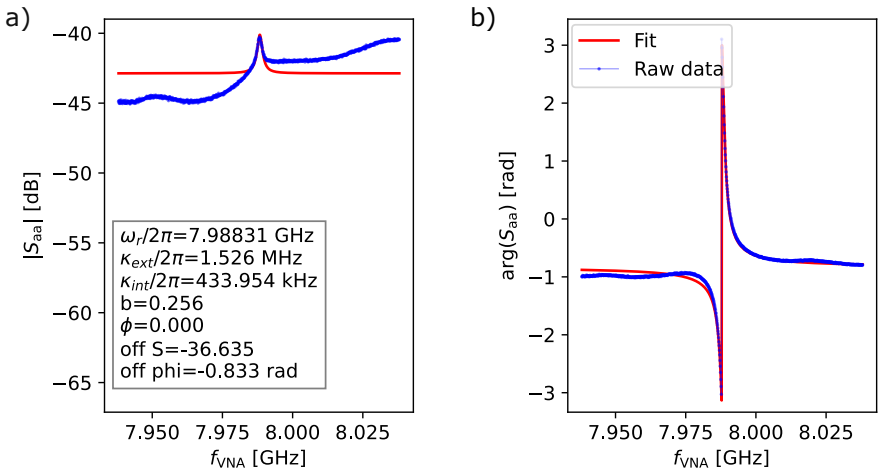

Figure 11: Fano reflection in a) amplitude and b) phase of the reflection coefficient observable in *Res* 1 *d*. Here the b and Φ factors are imperfection dependent.

Res 2

On sample Res 2 both resonators are working correctly, one with fundamental mode at 4GHz and one at 10 GHz. Since I was interested in obtaining coupling with resonators with very low frequencies I focused more on the 4 GHz resonator, being able to access higher harmonics.

Resonator	Expected frequency (GHz)	Frequency (GHz)	κ_{ext} (kHz)	κ_{int} (kHz)	b
e -$\lambda/2$	4	4.01570	182.908	112.869	0.303
e -λ	8	8.00122	911.110	192.734	0.127
e -$3\lambda/2$	12	11.98658	402.791	259.962	0.252
f -$\lambda/2$	10	9.98460	3828	1022	0.200

Table 4: Modes on Res 2. Factors κ_{ext}, κ_{int} and b are reported. Special attention is to be address to the 3rd harmonic clearly observable on the 4 GHz resonator with quality factor Q = 10^6.

Looking at data in Tab. 4 it is noticeable that the meandered resonators implemented very clean modes frequencies, with κ_{ext} in the kHz range, meaning a Q_{ext} of the order of 10^6, for the low frequency modes. They also allowed to observe very clean modes with same order of magnitude for the quality factor at higher harmonics, allowing the handling of two modes on the same resonator in the 3-15 GHz bandwidth, notably the $3\lambda/2$ mode at 11.987 GHz for resonator *e*. Finally higher quality factors were reached while keeping the overcoupling.

The results drawn from this sample generation confirmed the validity of meanders intro-

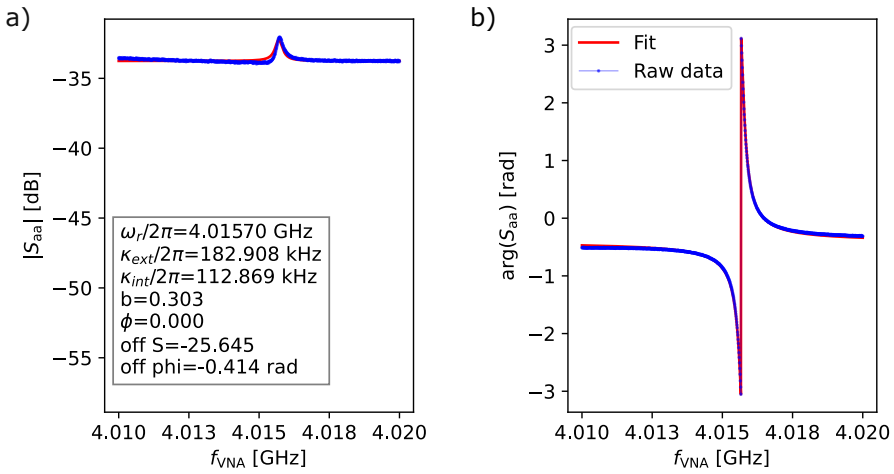

Figure 12: Reflection coefficient a) amplitude and b) phase measurement at low power RF input signal on the 4 GHz fundamental mode of *Res* 2 *c*. Fano asymmetry was compensated in data analysis obtaining the correction factor *b*.

duction in the CPW resonators design, establishing a reliable method to address two of the goals of my internship: the higher quality factor and lower frequencies of the fundamental mode to observe also the $3\lambda/2$ mode with the same high Q_{ext} value. The obtained success provided the foundation for the fabrication of the last generation sample, in which parametric coupling via a JPC would be introduced. The findings from the described analysis allowed to define the meandered design as the standard one for subsequent generations.

3.3 Third generation: JPC 3

The final generation combined previous advancements in design i.e. the holes in the ground plane and the meandered resonators, into a full JPC system intended to demonstrate parametric coupling. This chip also served as a diagnostic platform, including multiple test structures enabling investigation analysis on fabrication and component behavior:

- Meandered $\lambda/2$ Nb resonator (labeled Full Nb in Figure 13) with a target fundamental mode at 4 GHz fundamental mode to get a reference mode spectrum.
- A resonator with a single Al patch (labeled Al patch in Figure 13) to test the hypothesis that the Nb/Al contact could induce losses reducing the quality factor. It was not analyzed since due to some problem during electronic lithography the Al patch was not realized.
- A resonator with a single Josephson junction (labeled Single JJ in Figure 13) to test its effect on resonance frequency.

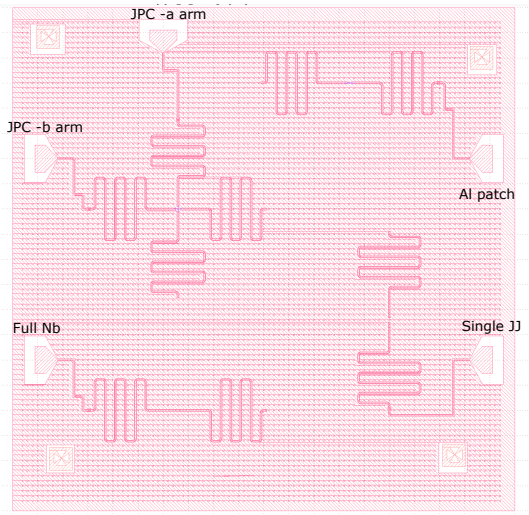

Figure 13: Design of JPC 3 included three diagnostic structures - a Nb resonator at 4 GHz (Full Nb), a non working Nb resonator with an Al patch due to electronic lithography problem (Al patch), and a resonator with a single Josephson junction (Single JJ). The main structure on the chip is a full JPC with an unshunted JRM of 40x40.8 μm^2 surface, larger than the ones in JPC 1 and JPC 2 in order to increase its sensitivity to magnetic flux, and junctions bridges of 0.4 μm width and of 1.3 μm length. The two arms of the JPC were targeting fundamental modes at 4 GHz and 4.5 GHz. No DC flux line is present on this sample.

3.3.1 First cool down

Initial measurements of JPC 3 (Figure 13) revealed clearly defined modes both in reflection and transmission spectra. Since on the JPC we were introducing the Josephson ring, that adds inductance in series with the resonators ones, they should be taken into account. The overall inductance of each arm will be increased and thus the modes frequencies were expected to be lowered, redshifted, of an amount due to the participation ratio, $\sim$ 10% or lower for our measurements (See eq. 5).

From data in Table 5, about the testing components on this sample, we can say that the pure Nb resonators exploited the same results described in section 3.2.1 about the second generation experiments, giving a good reference spectrum for JPC modes. Instead the resonator with the single Josephson junction exploited only one mode at 8 GHz that was not showing Kerr effect, meaning that probably the junction fabrication was not successful and so it was short circuiting the device. Finally on the JPC we see three modes available on each resonator at $\sim$0.5 GHz lower frequency than the targeted ones, confirming the reduction of frequencies due to the presence of the inductance of the ring, also confirmed by the appearance of Kerr effect while sweeping power - frequencies are lowered as the input signal power is increased and the reflection coefficient amplitude tends to decrease. Figure 14 shows one example of the power sweeps that were obtained from this sample. Here the expected jump in frequency between two different stability states, due to a change in photon number in the mode, is observable. The measured frequency lowering is systematic on JPC modes and it

Resonator	Expected frequency (GHz)	Frequency (GHz)	k_{ext} (kHz)	k_{int} (kHz)	b	Kerr effect	Transmission
Full Nb-$\lambda/2$	4	4.0086	286.801	106.001	-	-	-
Full Nb-λ	8	8.00565	742.650	11.239	0.230	-	-
Full Nb-$3\lambda/2$	12	11.98783	707.074	100	-	-	-
Single JJ	4	8.00634	356.549	217.299	0.250	-	-
JPC-a-$\lambda/2$	4.5	4.09619	440.252	257.521	-	yes	yes
JPC-a-λ	9	8.45147	571.736	1529	-	-	yes
JPC-a-$3\lambda/2$	13.5	12.96047	3113	3671	-	yes	yes
JPC-b-$\lambda/2$	4	3.59352	209.840	195.556	-	yes	yes
JPC-b-λ	8	8.45150	723.895	1270	-	-	yes
JPC-b-$3\lambda/2$	12	10.24802	4219	1946	-	-	yes

Table 5: Modes on JPC 3 sample. All the expected modes on the JPC are clearly observable at slightly lower frequencies than the expected ones due to the presence of the JRM, with participation ratios even lower than 10%. The most concerning data is the quality factor associated to the 3rd harmonic modes, since again it is almost 10 times higher than the one for the $\lambda/2$ mode. This is expected due to higher frequency. On this sample also Kerr effect and transmission coefficient have been probed.

describe a participation ratio of the ring coherent with the theoretical one, expected from eq. 5. The Kerr effect is observable on all the modes of both arms of the JPC even if the 3rd harmonic on the b arm was harder to detect and it shows a far higher lowering in frequency of about 2 GHz and a quality factor of 10^3 (see Table 5 JPC-b-$3\lambda/2$ mode), far lower than for the other detected modes. Finally the two λ modes are coincident with each other, 8.4514 GHz and 8.45150 GHz , emerging as a common mode between the two resonators.

The obtained results were cross-validated by measuring the transmission coefficient as well. If also transmission showed the same peaks then the observed modes are the real ones and not just some spurious harmonics or noise and the same modes were validated.
Having such good real modes allowed thinking that they could have also nice behavior in flux and so that parametric coupling could be possible. During this first cool down, we realized that we could not apply the magnetic field on this sample directly, since no DC flux line was available on it and because the sample holder we used had the Al cap. Aluminum being superconductor, it expulses the magnetic field, so even with the addition of an external coil directly on top of the JPC no flux dependence was observed.
Thus we decided to cool down the sample a second time applying flux with an external magnet.

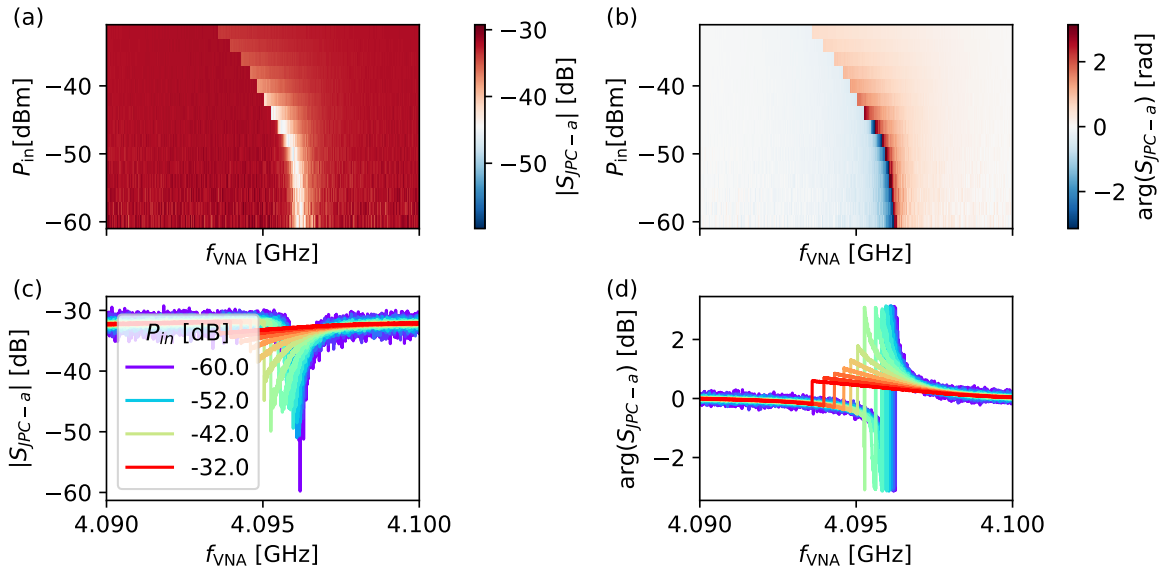

Figure 14: Reflection coefficient measurement of the $\lambda/2$ mode of a arm of the JPC on sample JPC 3. It is clearly visible that the mode frequency expected at 4.5 GHz is a bit lowered due to the JRM. (a) Reflection coefficient amplitude a nd b) phase as a function of input power and frequency, the shift due to input signal variation towards lower values is observable. (c) Reflection coefficient amplitude as a function of frequency. Different input power are represented in differently colored curves and from those the abrupt jump, due to the change in photon number, between two stability states is clearly noticeable. (d) Reflection coefficient phase showing the same jump as (c) and that the jump is sharper with higher power.

3.3.2 JPC 3 - second cool down

To confirm the flux tunability an external magnet was used to apply a magnetic field in the range ± 10 mT allowing to observe the expected flux dependence, with periodicity due to flux biasing in reflection coefficient behavior, as shown in Figures 15 and 16. Here the expected hysteresis due to the nonlinear Josephson dynamics of the JPC is showed. The JRM effective inductance (eq. 3) depends on the external flux and becomes multivalued when it approaches half a flux quanta (2π) leading to a bifurcation that reflects in the hysteresis of the frequency when flux is swept up or down (further explanation on this feature can be found in [3]). Since the sample is outside of the magnet it does not perceive the applied field but much less and it can be computed from flux quantum and ring surface as $B = \frac{n\varphi_0}{A}$ with n being the number of flux quanta threading the ring.

The presented result has been obtained for all the modes that we found on the JPC in sample JPC 3, presented in Table 5, confirming that the JPC was working in the expected nonlinear regime allowing for parametric coupling. The successive step of attempting to obtain the three-wave mixing via pumping, looking for modes amplification and conversion, was justified.

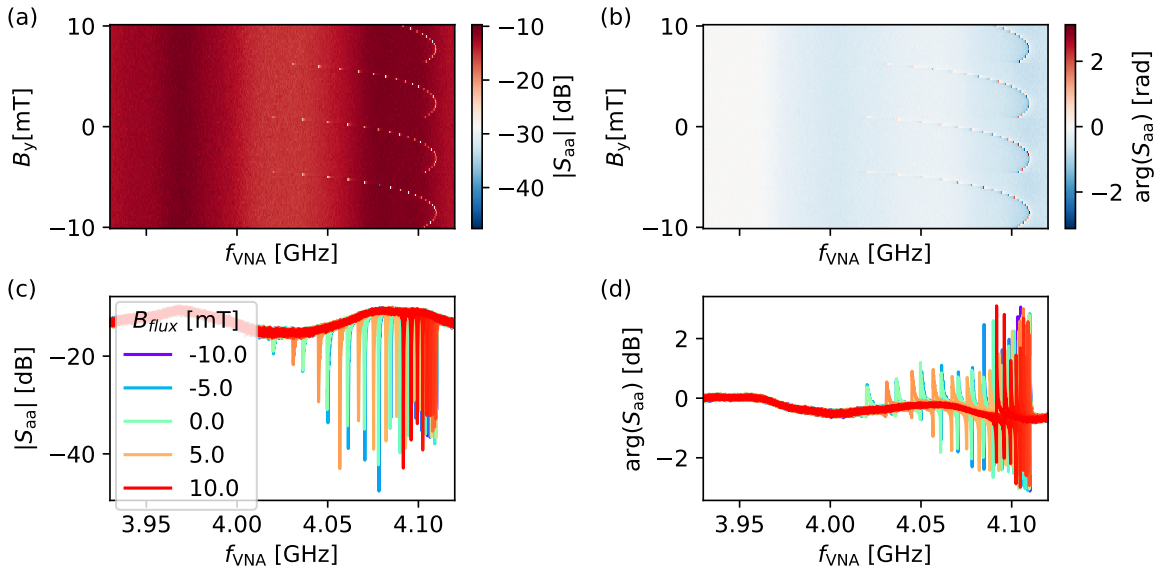

Figure 15: Flux dependence of the resonant frequency of the $\lambda/2$ mode of a arm of JPC 3 showing the expected periodic behavior. a) Reflection coefficient amplitude and b) phase as a function of frequency and magnetic field, sweeping it from 10 to -10 mT, showing the jump from the metastable to the stable three-wave mixing configuration of the JPC, exploiting the periodicity. c) Amplitude and d) phase of the reflection coefficient as a function of frequency, different applied magnetic field are highlighted with different color curves.

3.3.3 Parametric interactions

With the mode spectrum and flux dependence verified, the next objective was to probe the parametric interactions using the three-wave mixing process, through the expression of modes amplification and conversion.
The JPC is commonly used as a quantum limited amplifier through the application of a time-dependent pump driven far off-resonance on the common mode of the mixer. This pump is able to distinguish particular operating modes of the device, observable in expression 7 where the c mode is substituted now with the pump value p.
When the pump is applied to the sum of the frequencies of the two modes of the JPC we want to couple, $\omega_p = \omega_a + \omega_b$, the Hamiltonian will describe a total parametric interaction:

$$\hat{H}_{ampl} = \hbar\chi|p|\left(\hat{a}\hat{b} + \hat{a}^\dagger\hat{b}^\dagger\right) \tag{14}$$

where the coupling strength can be expressed as a function of all the participation ratio and mode frequencies:

$$\chi\,|p + p^*| = \frac{1}{4}\sqrt{\xi_a\xi_b\omega_a\omega_b} \tag{15}$$

that is for the unshunted version of the ring, using a flux value, φ_{ext}, which correspond to the starting point of the non-linear behavior of the device, being sure to be in its stability region.
Applying the rotating wave approximation for which only the slowly rotating terms are kept, we can use the previous expression to describe coupling and creation of an entangled state

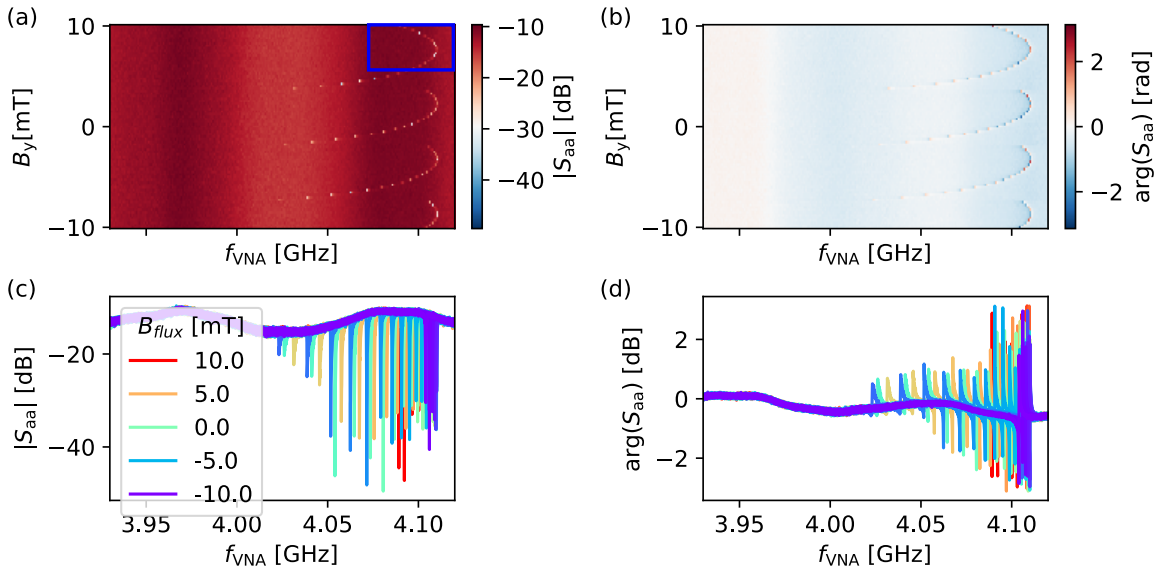

Figure 16: Flux dependence of the resonant frequency of the $\lambda/2$ mode of a arm of JPC 3 showing the expected periodic behavior. a) Reflection coefficient amplitude and b) phase as a function of frequency and magnetic field, sweeping it from -10 to +10 mT, it showed a parabolic shape rather than a jump at high flux, highlighted by the blue square. This is due to the fact that the magnetic flux setting needed to go from 10 mT to -10 mT (in one step) before starting the measurement, taking also the values for the sweep in the other direction. This shows that at 10 and -10 mT the frequency assumes the same values and so the right behavior of the unshunted JPC is obtained. c) Amplitude and d) phase behavior of the reflection coefficient with frequency, magnetic field impact is presented in curves with different colors.

between the two resonators of the JPC. This will result in eq. 14 that describes the exact behavior of the JPC as a parametric amplifier when a signal is sent from the input ports of the a or b modes. If these two modes are driven only by vacuum fluctuations, their output fields will be in an EPR (Einstein-Podolsky-Rosen) superposition state

$$|EPR\rangle = e^{ra^\dagger b^\dagger - r^* ab}|0,0\rangle \tag{16}$$

where r is a squeezing parameter. The previous Hamiltonian takes also the name of two-modes squeezing Hamiltonian for this reason.
Expression 14 means that whenever we are sending a signal through the pump, we are creating a photon in the two resonators destroying one in the pump, giving rise to the parametric amplification and if this happens when the resonators are in vacuum state we are actually creating quantum-correlated radiation at the two frequencies, the entanglement between the two photons is created, resulting in the origin of the EPR state: a two mode squeezed state. To experimentally verify this behavior the pump signal was connected to the input port on the a mode and the output power associated to the mode on the output port on a was measured through a Power Spectrum Analyzer (PSA). With this configuration the amplified response was too low to be observed, so we slightly populated with photons the other mode

using a driving signal on the b arm input. This allowed to have a more intense amplification effect, observable in Figure 17. In this figure we see a bright peak value in correspondence

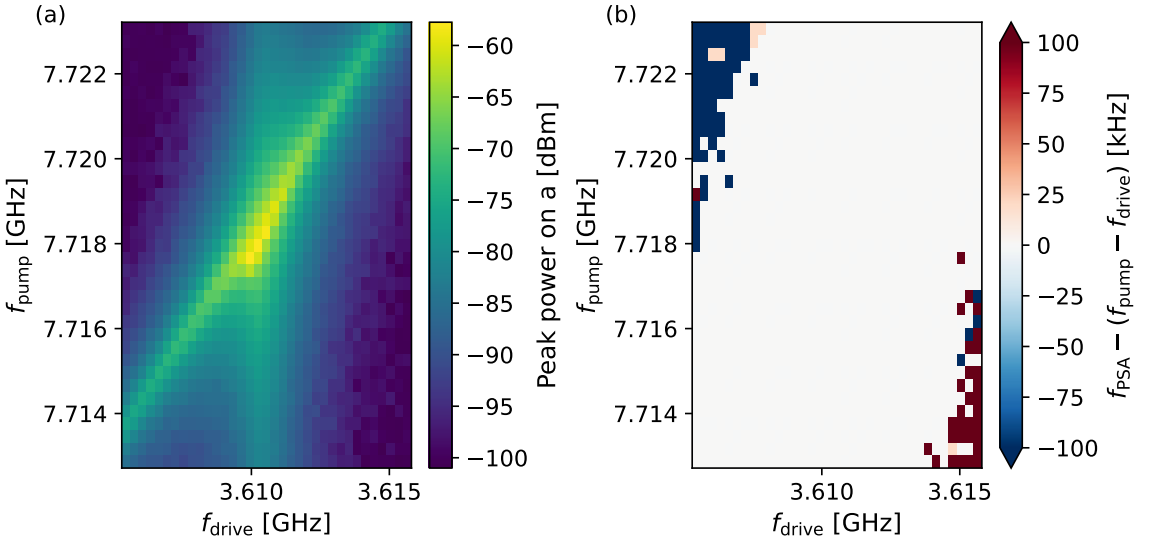

Figure 17: Output power from amplification between $\lambda/2$ mode at $\sim$ 4.1 GHz and $\lambda/2$ at $\sim$ 3.61 GHz on the JPC on sample JPC 3. a) Output power peak associated to the 4.1 GHz mode as a function of the pump and other mode driving frequency. The inclined green line confirms the respect of the amplification requirement on ω_p pump frequency, so if it is increasing, the driving signal is increasing to since the output mode frequency is fixed. The observable vertical shadow is just the resonance frequency of the driven mode. b) Plot of the difference between the frequency value on the PSA and the difference of the pump and driving frequencies. The central white part showed that this value was zero and so that the right frequency on PSA was being visualized and that the requirement for amplification was being respected.

of the resonance frequency of the driven mode and a pump value ,$\sim$ 7.71 GHz, that is the sum of the two used modes resonance frequencies, in this case the two $\lambda/2$ at 4.09 GHz and 3.61 GHz. Furthermore, we can see the linear behavior of the pump frequency and driving frequency, meaning that when the value of the pump is increasing also the driving one is growing maintaining the requirement for amplification true, since the other mode frequency is fixed.

Similarly, if we pump the input signal at $\omega_p = \omega_a - \omega_b$, the difference of the two modes of the resonators, the interaction described by the Hamiltonian (in the RWA scheme) becomes the one of a parametric frequency conversion:

$$H = \hbar\chi|p|\left(\hat{a}\hat{b}^\dagger + \hat{a}^\dagger\hat{b}\right) \tag{17}$$

In this expression it is noticeable how a photon can be converted from one resonator to the other. When destroying it in one resonator it is created in the other at a different frequency, creating a coherent coupling between the two resonators states.

4 Fabrication process

The fabrication of superconducting quantum circuits involve a multi-step workflow requiring high precision, cleanroom environment and cryo-compatible materials.The samples described in previous sections were fabricated on a chip of 10x10 mm^2 realized from a Silicon wafer of 280 nm thickness on top of which 250 nm of Niobium have been deposited by sputtering. The wafer was then cut into squares using a diamond saw.
The goal was the realization of resonators with transmission lines and the Josephson junctions ring. The two parts were realized with different methods since they needed different precision and resolution.

4.1 Nb etching

The first step of the fabrication process had the goal of etching the Nb to create resonators and their transmission lines. To achieve this result optical lithography was used.
The first step is to deep clean the substrate with acetone and isopropanol in sonication for 5 minutes and then using plasma cleaning process, with Oxygen, for other 5 minutes; in this way we are sure that dusts from previous processes are not present on it. After that a layer of SPR 1.0 700 is spin-coated and baked for 1 minute at 95°C.
At this point, a mask of the same kind of the one presented in Figure 18 is exposed by optical lithography to print the pattern on the resist, in order to obtain the contact pads, transmission lines, coupling capacitances and the resonators. After a first resist development in MF319 for 45 seconds, Reactive Ion Etching (RIE) is used to remove Nb from the exposed region of the sample, exposing Si to the environment. To be sure of this result the reflection of a laser beam on a specific region of the sample is observed: having Nb and Si different reflection properties, the intensity of the reflected beam will decrease while exposing Si rather than reflecting on Nb, due to the presence of the native Si-oxide layer underneath it. To be sure that the entire oxide and Nb layer have been removed the sample is over-etched for a couple of minutes until the beam intensity starts increasing again, meaning that the laser beam is encountering Si. In the end resist is completely removed using a specific PG remover by submerging the sample in it overnight, or for a couple of hours, at 60°C heating. Finally, the sample is sonicated for 5 minutes while still in the remover, rinsed with IPA and dried with a Nitrogen gun.

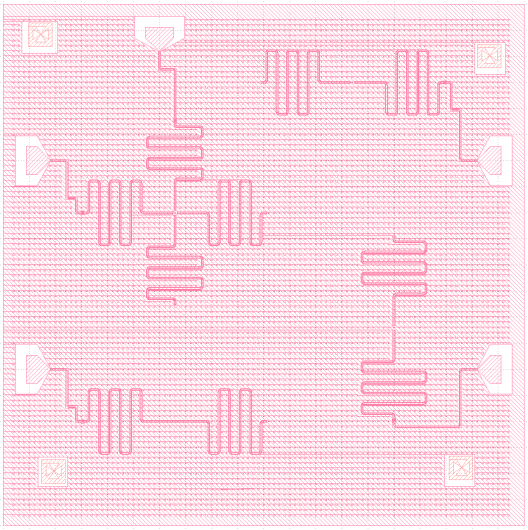

Figure 18: Design used to generate the pattern mask for the optical lithography. The JPC 3 design is used as an example on which all the implemented design features are observable. We can see the alignment crosses to simplify the alignment of the the electronic lithography pattern in the successive step, the meandered resonators and the ground plane holes.

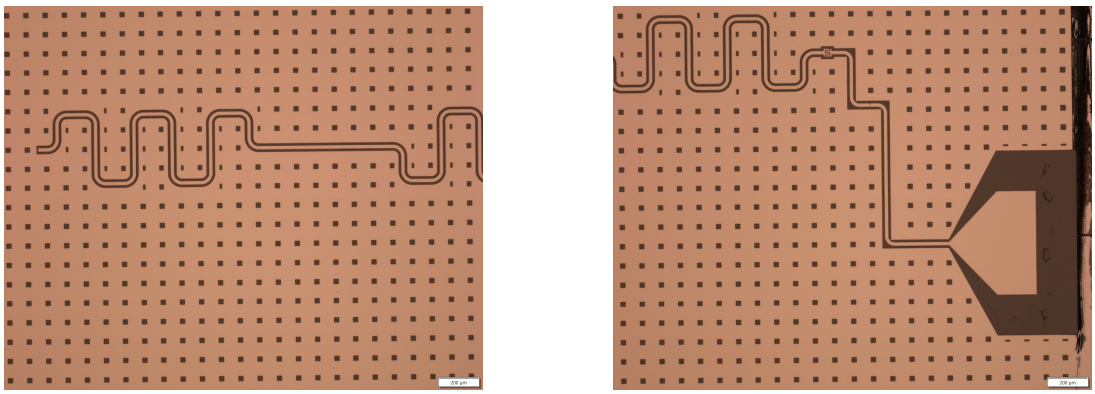

(a) Meander resonator after Nb etching.

(b) Contact pads and coupling capacitance after Nb etching.

Figure 19: Microscope images of sample Res 1 of a) meandered resonator and b) contact pads and coupling capacitance detail after optical resist development and Nb etching.

4.2 Josephson ring fabrication

The second stage involved patterning of the Josephson ring using the technique of Dolan Bridges. This method consists in creating suspended bridges of electronic resist and then evaporate with two opposite angle the desired material to obtain the junction, with an interval between the two depositions, to allow the oxidation of the first layer and thus create the insulating oxide layer: Superconductor/insulator/superconductor is the wanted layered structure that for us correspond to Al/AlO_x/Al since Al is superconductive with a critical temperature of Tc = 1.2 K.

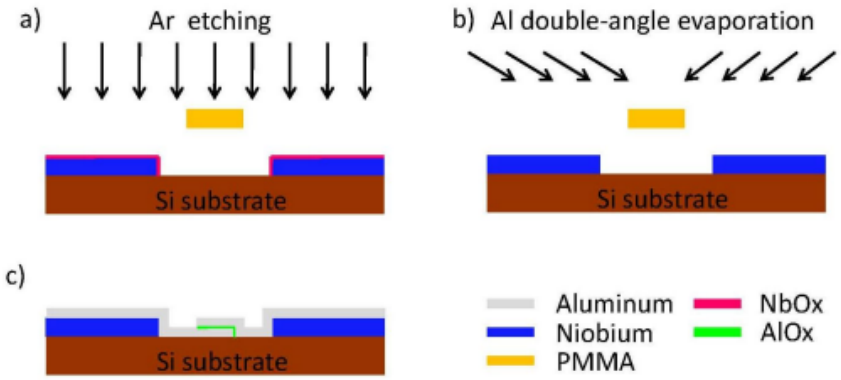

Figure 20: (a) Argon etching is used to remove the NbO_x on the surface of the patterned substrate to allow for the best Al adhesion on it. (b) The double-angle evaporation is executed; between the two layer deposition the Al-oxidation step is performed. (c) The PMMA mask is removed through a development step. In this picture the green line in between the gray layers is the AlO_x.

The process started with the deposition of three layers of resist: two layers of MMA, for a total thickens of 400 nm and one of PMMA, with thickness of 100 nm. Two different resists are used because of their distinct electronic properties and the need for different exposure and successive development times to be patterned. This allows us to generate the suspended PMMA bridge taking advantage of the MMA higher sensitivity to electrons. Indeed, MMA is more exposed to electrons back-scattered from the substrate, constituting them the two bottom layers, generating thus an undercut to the PMMA layer during the development step. The PMMA, being the top layer, is less exposed to back-scattered electrons, defining thus a larger area that will define later the surface of the junction.

Once the ring has been exposed with an electron beam, it is developed and an hard PMMA mask, with suspended bridge where the junctions should be grown, appears. Thanks to this mask the evaporation with two equal but opposite direction angles is performed:

- First Al layer deposition.
- About 5 mbar of oxygen are inserted in the chamber (7 minutes of oxidation) to allow the oxidation of the deposited Al layer.
- Second Al layer deposition.
- Oxygen capping to prevent air contamination.

The purpose of using angle at 35° with respect to the normal direction allow us to take advantage of the suspended bridge shadow and generate thus the junction with the wanted surface. All the procedure steps are described in Figure 20 and the precise workflow is reported in Appendix A.

At this point the entire chip is covered in Al that must be removed using a lift-off procedure. The sample is left for 45 min - 1 h in heated acetone at 60°C and then when Al surface gets wrinkled we use a pipette to spray room T acetone on top of it to remove the excess part, being careful in not letting any of the lifted Al to fall back onto the sample, otherwise it will stick there. Once we are sure to have removed all the excess parts of Al, the sample is rinsed in IPA and dried with a Nitrogen gun.

We now have a finished device ready to be characterized and tested.

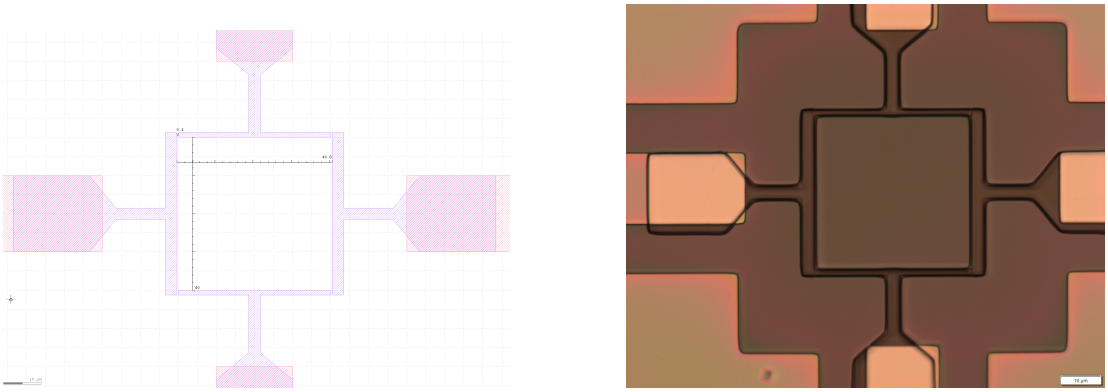

(a) Josephson Ring Modulator design.

(b) JRM after development after electronic lithography.

Figure 21: Mask for the electronic lithography for Josephson Ring Modulator exposure. a) The ring design is presented with the used dimensions. b) Result of the electronic lithography with x100 magnification on sample JPC 3. Here the Josephson junctions can be seen playing with the focus parameter of the microscope.

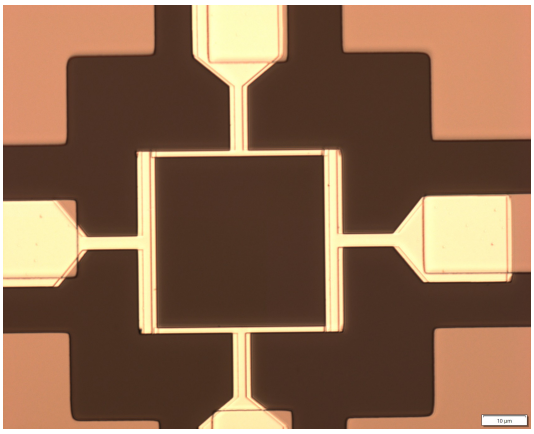

Figure 22: Finished device after Al lift-off. In the picture the unshunted Josephson ring modulator on the JPC of sample JPC 3 is visible.

5 Measurement in a cold environment

All the performed measurements needed a cold environment due to two main reasons:

- Working with Josephson junctions made of Aluminum, to enter the superconducting regime temperature below 1.2 K (Al critical temperature) must be reached.
- Quantum states must be protected, so the thermal energy must be much smaller than the energy gap, $\hbar\omega > k_B T$, defining the necessity of reaching T$<$ 100 mK since ω is of the order of GHz. This will keep thermal photon population the lowest as possible.

To be able to address this temperature value a dilution fridge was used (see Figure 23a for its scheme). The used fridge reaches $\sim$ 10 mK ensuring to be below the Aluminum critical temperature, allowing the study of resonators behavior and the coupling process in JPC.

5.1 Cabling

To position the chip inside the fridge it is fixed at the center of a sample holder by four little clamps on the corners, visible in Figure 23b. Once the sample has been stabilized in the holder it is possible to create connections between the Printed Circuit Board (PCB, made of gold) and the chip using Al wire. This allows us to create some connections between the holder and the chip pads allowing signal transmission from the fridge line to the device on the chip. All of this is possible thanks to SMP connector on top of the sample holder and SMA ones for external cabling. On the chip two different kinds of bonds can be identified: there are bonds over each resonator that connect the ground plane, making it homogeneous, and there are distinct ones between the contact pads and the PCB circuit for connection (see Figure 23c).
To connect the sample with external measurement set-up directional coupler were used. Those allowed reflection measurements limiting the noise on the output signal with respect to the input one. This is possible since directional couplers part the reflected signal of the resonators from the input one, distinguishing RF signal depending on their propagation direction. The reflected signal is sent to a different coaxial cable with less noise, with respect to the one for the input signal. Before exiting the fridge the signal is amplified at low T to improve the signal to noise ratio.

Two other important elements that must be eventually introduced in the fridge cabling are the cryoperm magnetic shield and the external magnet. The cryoperm magnetic shield is made of cryoperm, a material made prevalently of Nickel but with the addition of copper able to screen magnetic fields in cryogenic temperatures. During my set of measurement it was needed during flux application across the JRM when using a DC drive line due to some offset in the field induced by the elevator that is right next to dilution fridge.

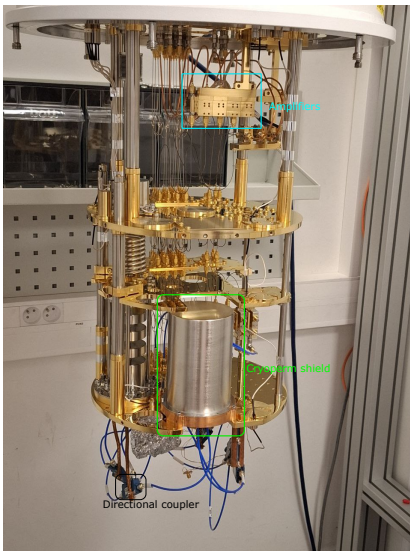

(a) Dilution fridge cabling with labeled components: amplifiers (blue), cryoperm shield (green), and directional couplers (black).

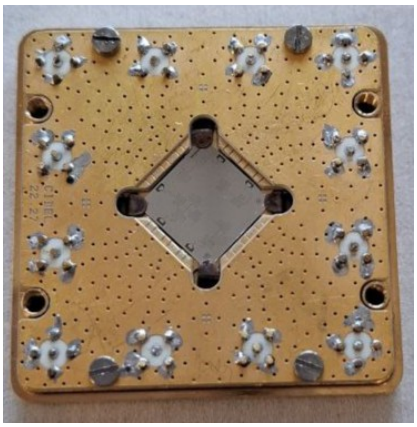

(b) Sample holder with four visible clamps securing the chip.

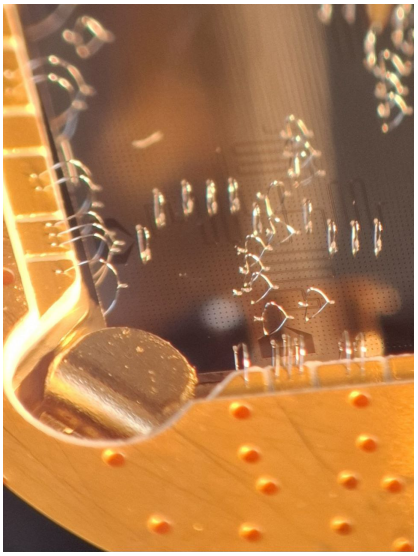

(c) Microscope image of the Al bonds on a sample.

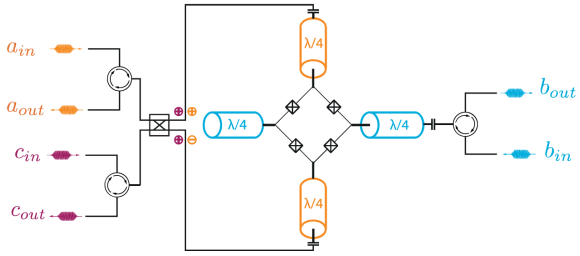

(d) Schematic of the electrical connection inside the cryostat.

Figure 23: Experimental setup. (a) Internal cabling of the dilution fridge. (b) Sample holder used for chip installation. (c) Microscope image of a sample showing the two types of Al bonds: PCB to chip and chip to chip. (d) Electrical schematic of the connections inside the cryostat.

6 Conclusion and future perspective

This project presented the design, fabrication and cryogenic characterization of a superconducting device for parametric coupling with the long-term goal of advancing the implementation of scalable quantum neural networks. The focus was on optimizing resonators quality factor and demonstrating parametric coupling with more than two modes, through a Josephson Parametric Converter. This work represents a big step in bridging the theoretical and simulation side of quantum neural networks and its experimental applications. I was able to enable long coherence time by fabricating high-quality superconducting resonators with meandered coplanar waveguide, that is optimal for the memory requirement of neural networks. Furthermore, the use of JPCs to create entangled state through three-wave mixing was successfully validated with the observation of two-mode squeezing.
This results provided promises of superconducting circuits for neuromorphic applications:

- Quantum neurons with bosonic modes: JPC parametric coupling enabled controllable interactions between quantum neurons, each of the available oscillator, mirroring the tunable synaptic weights of classical network. This leads to the next major researcher objective: implementation of training protocols within the quantum hardware.
- Scalability: the needed trade-off between connectivity and physical resource demands in classical neural network is overcame by the exponential state space provided by superconducting resonators and microwave photons dissipating 10^{-22} J per operation.

Looking ahead from this results, several direction emerges for possible implementation of such a device:

- Kerr non-linearity can be used as a physical activation function. In the quantum setting, Kerr effect can be tuned via circuit parameters or flux bias (tuning Kerr coefficients) allowing for real-time reconfiguration of nonlinearity strength, enabling adaptable computational behavior in QNN
- Enhanced readout via transmon coupling: the perspective of the JPC studied in this work is to be integrated with transmon quibit developed by my colleague Briac Flesselles to enable high-fidelity, quantum non-demolition, readout of resonators states. In this configuration a Transmon can dispersively be coupled to a resonator mode allowing measurement of photon number without collapsing its quantum state (See [6])

These direction point toward a hybrid architecture combining bosonic modes, parametric tunability and qubit-assisted readout, a powerful platform for future experiments in quantum learning and neuromorphic computing.

A Fabrication Recipe

Cleaning step

- Sonication in acetone bath for 5 minutes
- Sonication in Isopropanol (IPA) bath for 5 minutes
- Plasma cleaning with 50 % power, 10 sscm O_2 for 5 minutes

Optical lithography

- Resist spinning
  - Pre-baking the sample at 95° for 1 minute
  - 3 drops of SPR 1.0 700, spin for 30 s with speed = 4000 and acceleration = 4000
  - Baking at 95° for 1 minute
- Projection lithography
  - Design conversion: high resolution, $\Delta x = 0$, $\Delta y = 0$, antialisying = 2
  - Exposure: high resolution, 0.4 s and power 12
- Development:
  - MF319 for 45s
  - Distilled water 5s

Reactive ion etching

- 40 sccm FS_6, 20 sccm O_2 until the reflected laser intensity start decreasing for the second time
- Etching chamber cleaning
- Resist removal
  - PG remover at 60° over night (or a couple of hours)
  - PG remover in sonication for 5 minutes
  - Rinsing in IPA
- Plasma cleaning

Electronic lithography

- Electronic resist spinning:
  - Pre-baking 1 minute at 185°C
  - 3 drops of MMA EL 10, spinning 60 s, speed = 4000, acceleration = 4000
  - Baking 3 minutes at 185°C

  - Cool-down 1 minute
  - 3 drops of MMA EL 10, spinning 60 s, speed = 4000, acceleration = 4000
  - Baking 3 minutes at 185°C
  - Cool-down 1 minute
  - 3 drops of PMMA A-4, spinning 60 s, speed = 4000, acceleration = 4000
  - Baking 15 minutes at 185°C

- Electron beam exposure:
  - Aperture: 10 μm
  - Energy: 20 keV
  - Step size area: 0.004 μm^2
  - Dose: 270 $\mu C/cm^2$

- Development
  - MIBK/IPA solution 45s
  - IPA

Evaporation

- Ti pump 100 nm with rate 0,5 nm/s
- Ion mining 250 V, 8 mA, 15s, ±35°
- Al evap at rate 1 nm/s at -35°, 53 nm deposited thickness
- O_2 oxidation MP= 5,08 mBar 7 minutes
- Al evap at rate 1nm/s at +35°, 103 nm deposited thickness
- O_2 capping HP = 20 mbar 5 minutes

Lift-off

- Acetone bath, heated at 60°C for 45 minutes
- IPA rinsing

References

[1] Carles B. Plouet E. et al. Dudas, J. Quantum reservoir computing implementation on coherently coupled quantum oscillators. *npj Quantum Inf 9, 64 (2023).*, https://doi.org/10.1038/s41534-023-00734-4.

[2] V. E. Manucharyan et al. Rf bifurcation of a josephson junction: microwave embedding circuit requirements. *arXiv:cond-mat/0612576, (2006)*, https://doi.org/10.48550/arXiv.cond-mat/0612576.

[3] Emmanuel Flurin. The josephson mixer : a swiss army knife for microwave quantum optics. *Quantum Physics [quant-ph]. Ecole normale supérieure - ENS PARIS, 2014. English.*

[4] Elie Gouzien Julie Grollier Danijela Marković Julien Dudas, Baptiste Carles. Training the parametric interactions in an analog bosonic quantum neural network with fock basis measurement. *arXiv:2411.19112 [quant-ph], (2024)*, https://doi.org/10.48550/arXiv.2411.19112.

[5] D. Rieger, S. Günzler, M. Spiecker, A. Nambisan, W. Wernsdorfer, and I.M. Pop. Fano interference in microwave resonator measurements. *Phys. Rev. Appl.20.014059, (2023)*, https://link.aps.org/doi/10.1103/PhysRevApplied.20.014059.

[6] Houck A. Schreier J. et al. Schuster, D. Resolving photon number states in a superconducting circuit. *Nature 445, 515–518 (2007)*, https://doi.org/10.1038/nature05461.

[7] Michel H. Devoret Uri Vool. Introduction to quantum electromagnetic circuits. *arXiv:1610.03438v2 [quant-ph], (2017)*, https://arxiv.org/pdf/1610.03438.

[8] L. Yu and Y. Yu. Energy-efficient neural information processing in individual neurons and neuronal networks. *J Neuro Res, 95: 2253-2266.,(2017)*, https://doi.org/10.1002/jnr.24131.